AGU PUBLICATIONS

JGR

Journal of Geophysical Research: Solid Earth

RESEARCH ARTICLE
10.1002/2017JB014907

Key Points:
- Transient plumes from Strombolian to Vulcanian explosions are described via high-speed visible light and thermal imaging
- Parameterization includes plume front velocity, velocity field, volume, apparent surface temperature, and ash eruption rate at vents
- Initial plume dynamic is controlled by number, source location, angle, duration, velocity, and interval between ejection pulses at vents

Supporting Information:
- Supporting Information S1
- Movie S1
- Movie S2
- Movie S3
- Movie S4
- Movie S5
- Movie S6
- Movie S7
- Movie S8
- Movie S9
- Movie S10
- Movie S11

Correspondence to:
P.-Y. Tournigand,
pierreyves.tournigand@ingv.it

Citation:
Tournigand, P.-Y., Taddeucci, J., Gaudin, D., Peña Fernández, J. J., Del Bello, E., Scarlato, P., … Yokoo, A. (2017). The initial development of transient volcanic plumes as a function of source conditions. *Journal of Geophysical Research: Solid Earth*, *122*, 9784–9803. https://doi.org/10.1002/2017JB014907

Received 23 AUG 2017
Accepted 19 NOV 2017
Accepted article online 27 NOV 2017
Published online 19 DEC 2017

The Initial Development of Transient Volcanic Plumes as a Function of Source Conditions

Pierre-Yves Tournigand[1], Jacopo Taddeucci[1], Damien Gaudin[1,2], Juan José Peña Fernández[3], Elisabetta Del Bello[1], Piergiorgio Scarlato[1], Ulrich Kueppers[2], Jörn Sesterhenn[3], and Akihiko Yokoo[4]

[1]Istituto Nazionale di Geofisica e Vulcanologia, Rome, Italy, [2]Ludwig-Maximilians-Universität, Munich, Germany, [3]Institute of Fluid Dynamics and Technical Acoustics, Technische Universität, Berlin, Germany, [4]Aso Volcanological Laboratory, Institute for Geothermal Science, Kyoto University, Kumamoto, Japan

Abstract Transient volcanic plumes, having similar eruption duration and rise timescales, characterize many unsteady Strombolian to Vulcanian eruptions. Despite being more common, such plumes are less studied than their steady state counterpart from stronger eruptions. Here we investigate the initial dynamics of transient volcanic plumes using high-speed (visible light and thermal) and high-resolution (visible light) videos from Strombolian to Vulcanian eruptions of Stromboli (Italy), Fuego (Guatemala), and Sakurajima (Japan) volcanoes. Physical parameterization of the plumes has been performed by defining their front velocity, velocity field, volume, and apparent surface temperature. We also characterized the ejection of the gas-pyroclast mixture at the vent, in terms of number, location, duration, and frequency of individual ejection pulses and of time-resolved mass eruption rate of the ejecta's ash fraction. Front velocity evolves along two distinct trends related to the initial gas-thrust phase and later buoyant phase. Plumes' velocity field, obtained via optical flow analysis, highlights different features, including initial jets and the formation and/or merging of ring vortexes at different scales. Plume volume increases over time following a power law trend common to all volcanoes and affected by discharge history at the vent. Time-resolved ash eruption rates range between 10^2 and 10^7 kg/s and may vary up to 2 orders of magnitude within the first seconds of eruption. Our results help detailing how the number, location, angle, duration, velocity, and time interval between ejection pulses at the vents crucially control the initial (first tens of second), and possibly later, evolution of transient volcanic plumes.

1. Introduction

Transient volcanic plumes are a common outcome from a variety of explosive eruption styles, including Strombolian, violent Strombolian, and Vulcanian, and can exhibit a variety of morphological features. The shape evolution of volcanic plumes holds key information on eruptive processes occurring at the vent and has been investigated at several volcanoes. However, our understanding of the link between source conditions at the vent and plume morphology and evolution is still far from complete, and theoretical and experimental models still require validation from field observations (Chojnicki et al., 2015a). In this study, we use imaging techniques to parameterize both source conditions and the initial growth stage of transient volcanic plumes from three different volcanoes showing a range of eruption styles.

Volcanic plumes consist in a mixture of ash, gas, and entrained atmospheric air that rises and expands in a turbulent flow including multiple vortexes. Bigger particles (>2 mm) can be part of this mixture in the early development stages. Volcanic plume dynamics have been theoretically divided into two end-members based on the ratio between the characteristic timescale of gas and ash injection (t_i) in the atmosphere and that required for the full rise and development of the plume (t_d) (Wilson et al., 1978). On one hand, steady state plume dynamics result from plumes that are fed by a sustained, constant-rate source ($t_i >> t_d$) (Morton et al., 1956). Such dynamics and the associated theory are commonly used to model large volcanic plumes released by Plinian eruptions (Woods, 1988). On the other hand, plumes formed by a quasi-instantaneous release of ash and gas ($t_i << t_d$), often termed "puffs" or "thermals", rise and grow following different dynamics (Turner, 1969). However, these two end-members often may fail to describe plumes from, for example, Strombolian to Vulcanian activity, in which the timescale of ash and gas release is of the same order of magnitude as that of plume development and rise. These intermediate plumes are generally named

"transient," and their evolution is strongly dependent on the specific, often unsteady or fluctuating, discharge history at the vent (Clarke et al., 2002).

Field observations have parameterized several aspects of transient plumes, including (i) plume rise velocity (Patrick, 2007; Patrick et al., 2007; Sahetapy-Engel & Harris, 2009; Webb et al., 2014; Zanon et al., 2009), (ii) volume (Delle Donne & Ripepe, 2012; Yamamoto et al., 2008) and temperature (Harris et al., 2013; Marchetti et al., 2009), (iii) air entrainment (Yamamoto et al., 2008), and (iv) exit velocities (Suwa et al., 2014). Two main dynamical stages are recognizable in most transient volcanic plumes (Patrick, 2007; Patrick et al., 2007). In the first stage, the evolution of the plume is dominated by the initial momentum of an eruptive vent (gas-thrust phase), while at a later stage plume rise is dominated by buoyancy originating from the entrainment and heating of the surrounding atmosphere (buoyancy-driven phase). In eruptions with transient plumes, pulsating behavior of ejection at the vent has been observed repeatedly (Capponi et al., 2016; Gaudin et al., 2017, 2014; Harris et al., 2012; Scharff et al., 2015; Taddeucci et al., 2012). Such unsteady vent discharge is expected to induce large changes on the resulting morphology and dynamics of plumes (Chojnicki et al., 2014, 2015a, 2015b; Clarke et al., 2002; Peña Fernández & Sesterhenn, 2017). However, the impact of specific discharge history on volcanic plume evolution has not yet been investigated in detail.

In order to provide new insights on the initial evolution of transient volcanic plumes in general, and on their link with vent dynamics in particular, here we focused on plumes from three different volcanoes: Stromboli (Italy), Fuego (Guatemala), and Sakurajima (Japan), covering a range of eruptive styles from Strombolian to Vulcanian. Eruptive plumes have been parameterized using a combination of high-speed visible light camera, thermal infrared camera, and high-definition visible light cameras. Videos were processed by classical and novel techniques, including optical flow analysis. Imaging the initial stages of plumes development provides a detailed characterization of the link between plume evolution and changes in eruptive vent dynamics.

2. Field Sites

2.1. Stromboli

Stromboli volcano is a 924 m above sea level (asl) stratovolcano located in the northeast part of the Aeolian Archipelago (Italy). The activity is characterized by intermittent explosions since at least the tenth century Common Era (Harris & Ripepe, 2007; Patrick, 2007; Rosi et al., 2013). During the period of recording in May 2013 (http://www.ov.ingv.it/ov/comunicati-stromboli/bollettino-2013-05-26.pdf) and May 2016, 9 to 12 events took place per hour from several vents hosted in the 300 m long crater terrace at ~800 m asl. This volcano serves as a reference for Strombolian activity due to its frequent explosions, accessibility, and vast literature on multiparametric investigations. Explosions from normal Strombolian activity, generally assumed to result from the bursting of gas pockets close to the top of a basaltic magma column inside the conduit, are divided into three main types: (i) gas dominated (Type 0), (ii) ballistic dominated (Type 1), and (iii) ash dominated (Type 2). The latter can be further subdivided into either ballistic rich (Type 2a) or ballistic poor (Type 2b) (Barnie et al., 2015; Del Bello et al., 2012; Francalanci et al., 1989; Leduc et al., 2015; Patrick et al., 2007; Taddeucci et al., 2015).

During two field campaigns in May 2013 and May 2016, 21 plume-forming ash-rich explosions (Types 2a and 2b), typically rising a few hundred meters above the vent, were filmed from three different locations (286, 370, and 542 m from the vent) (Figure 1 and Table 1).

2.2. Fuego

Fuego is a basaltic-andesitic 3,800 m asl stratovolcano in the central Guatemalan arc. Its activity varies between discrete Subplinian phases and continuous Strombolian to Vulcanian eruptions (Lyons & Waite, 2011; Lyons et al., 2010; Marchetti et al., 2009; Yuan et al., 1984). Explosions, originating from two main active vents (Lyons & Waite, 2011), are described as an abrupt ejection combined with a vigorous degassing lasting for several tens of seconds, generating plumes typically rising up to 1,500 m elevation above the source (Johnson, Aster, et al., 2004). At the time of our measurements the activity was characterized by several explosions per day forming ash plumes rising 400 to 1,000 m above the crater (Global Volcanism Program, 2012).

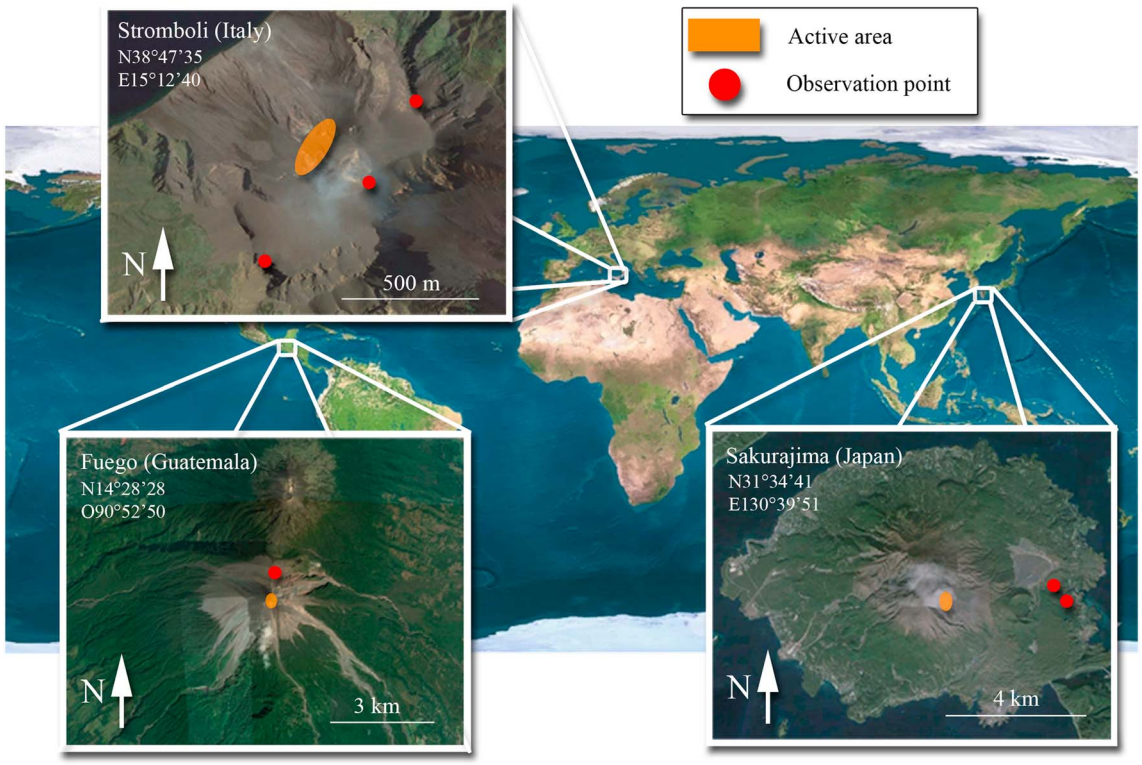

Figure 1. Map of the three different studied volcanoes, including the location of the active vent at the time of the field measurements (orange zone) and the locations of the cameras (red points). Coordinates refer to the vent area.

Eight videos were recorded from 968 m distance from the vent in January 2012 (Figure 1 and Table 1). The geometrical constraints of the field did not allow us to monitor the evolution of the largest plumes over a significant distance. Therefore, we focused this study only on the weakest plumes corresponding to the ones remaining within 200 m above the vent for the first 5 s of the explosion. This selection represents the low-energy end-member of activity of the volcano at the time of recording.

2.3. Sakurajima

Sakurajima is an andesitic, 1,117 m asl high stratovolcano in the southern rim of the Aira caldera (Kagoshima Bay, south Japan), composed of three different cones: Kitadake, Nakadake, and Minamidake (Iguchi et al., 2013; Ishihara, 1985). During July 2013, Sakurajima produced about 80 Vulcanian explosions within the month, generating ash plumes, mostly from Showa crater, rising from 1,000 to 4,000 m elevation above the source (Japan Meteorological Agency, 2016). Eruptions are driven by the accumulation of gas below a low permeable or impermeable plug of degassed, crystalline magma until the failure of the plug initiates the eruption (Iguchi et al., 2008).

We used 14 explosions from July 2013, occurring from the Showa crater, located at about 800 m elevation on the eastern flank of Minamidake, from two different observation points at 3.5 km distance from the vent (Figure 1 and Table 1).

3. Methods

3.1. Recording Setup

Videos were acquired using (1) a visible light high-speed camera (Optronis CamRecord CR600x2; 1024 × 1280 pixels definition, 500 frames per second (fps)), (2) a thermal infrared high-speed camera (FLIR SC655; 640 × 480 pixels definition, 50 fps frame rate, or 640 × 240 pixels, 100 fps), and (3) two wide-angle high-resolution visible-light Sony Handycam FDR-AX100 (3840 × 2160 pixels, 25 fps). FLIR and Optronis cameras were synchronized using a common trigger signal. Atmospheric correction of the thermal video was

Table 1
List of Explosions Presented in This Study

Date and hour	Explosion #	Camera	fps	FOV (m)	v_{max} (m/s)	v_b (m/s)	ED (s)
16/7/2013 09:30:00	Sa_1	Opt	500	209 × 167	187.1	8.0	9.5
		FLIR	50	928 × 696	153.0	10.8	9.5
15/7/2013 06:01:50	Sa_2	Opt	500	209 × 167	65.3	9.5	na
16/7/2013 01:24:10	Sa_3	Opt	500	209 × 167	149.1	11.4	na
		FLIR	50	928 × 696	124.9	12.4	na
19/7/2013	Sa_4	Opt	500	209 × 167	136.1	9.0	49.6
		FLIR	50	928 × 696	94.9	23.8	49.6
17/7/2013 22:29:00	Sa_5	Opt	500	209 × 167	134.8	na	na
		FLIR	50	928 × 696	89.4	12.8	na
17/7/2013 03:10:25	Sa_6	Opt	500	209 × 167	32.2	8.4	na
16/7/2013 06:56:22	Sa_7	FLIR	50	928 × 696	52.0	12.5	36.1
16/7/2013 08:31:51	Sa_8	FLIR	50	928 × 696	117.5	14.3	12.3
15/7/2013 05:11:10	Sa_9	FLIR	50	928 × 696	121.8	21.0	21.3
19/7/2013	Sa_10	FLIR	50	928 × 696	227.0	na	45.3
26/5/2013	St_1	Opt	500	37 × 30	51.2	10.9	na
26/5/2013	St_2	Opt	500	37 × 30	112.9	na	na
26/5/2013 12:12:31	St_3	Opt	500	37 × 30	53.7	na	5.6
		FLIR	50	307 × 230	54.7	10.2	5.6
26/5/2013 14:08:26	St_4	FLIR	50	307 × 230	68.7	14.4	3.0
26/5/2013 15:07:35	St_5	FLIR	50	307 × 230	52.3	10.0	1.5
26/5/2013 15:20:12	St_6	FLIR	50	307 × 230	62.9	15.0	2.0
26/5/2013 11:54:15	St_7	FLIR	50	307 × 230	77.7	12.9	3.5
26/5/2013 15:10:54	St_8	FLIR	50	307 × 230	33.2	9.4	4.2
22/5/2016 15:24:12	St_9	FLIR	50	307 × 230	25.3	6.7	23.5
25/5/2016 13:44:00	St_10	FLIR	50	450 × 338	24.8	8.4	5.6
		Sony	25	370 × 657	22.0	8.2	5.6
25/5/2016 14:42:18	St_11	FLIR	50	450 × 338	29.7	7.4	13.0
		Sony	25	370 × 657	13.8	7.0	13.0
		Sony	25	370 × 657	15.7	8.5	13.0
26/5/2016 14:09:07	St_12	FLIR	50	450 × 338	22.9	7.3	17.0
		Sony	25	370 × 657	27.4	9.4	17.0
		Sony	25	370 × 657	29.2	7.2	17.0
26/5/2016 14:32:56	St_13	FLIR	50	450 × 338	58.4	7.3	25.2
		Sony	25	370 × 657	45.0	7.3	25.2
		Sony	25	370 × 657	55.0	8.0	25.2
14/1/2012 16:11:05	Fu_1	Opt	500	128 × 102	35.5	9.1	5.1
		FLIR	100	428 × 161	31.1	7.9	5.1
14/1/2012 18:36:14	Fu_2	Opt	500	128 × 102	26.5	8.8	11.4
		FLIR	100	161 × 428	21.4	7.3	11.4
14/1/2012 16:48:20	Fu_3	Opt	500	128 × 102	64.4	11.8	na
13/1/2012 17:05:20	Fu_4	FLIR	100	96 × 255	48.0	14.2	4.7
14/1/2012	Fu_5	FLIR	100	161 × 428	22.4	10.1	3.3
14/1/2012 19:04:00	Fu_6	FLIR	100	161 × 428	70.4	na	10.2

Note. Key. Explosion #: Sa = Sakurajima, Fu = Fuego, St = Stromboli. Camera: Opt = high-speed, visible light range Optronis CR600x2, FLIR = thermal infrared FLIR SC655, Sony = high definition Sony FDR-AX100. Fps = Recording frame rate. FOV = horizontal and vertical field of view. v_{max} = maximum plume front velocity. v_b = average buoyant rise velocity. ED = estimated ejection duration. Videos from multiple cameras are occasionally available for one explosion (shaded lines). na, not applicable.

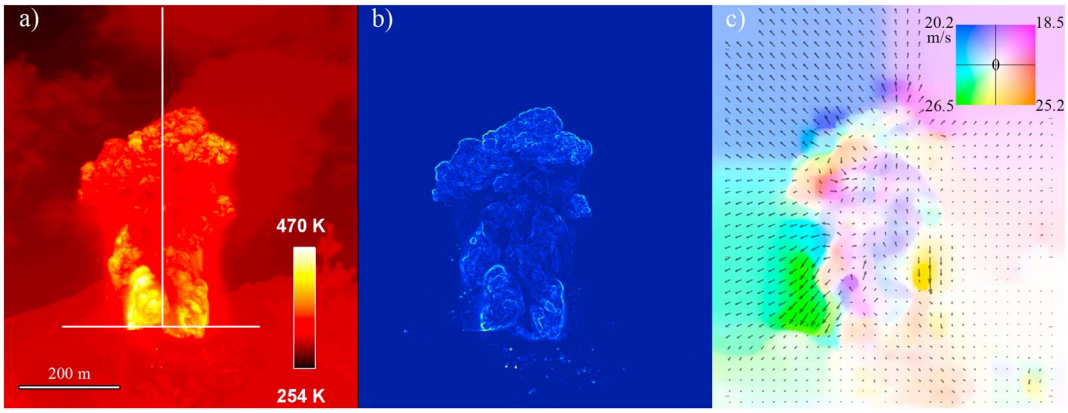

Figure 2. The Sa_7 explosion of Sakurajima. (a) The original, unprocessed thermal image (in color scale the apparent surface temperature). Horizontal and vertical temperature profiles along the white lines are plotted against time in Figure 5. (b) The same frame as in Figure 2a after pre-processing by thermal gradient and temperature threshold. (c) The optical flow results illustrating the projected (bidimensional) motion of the plume in the 0.2 s before the current frame (in color scale the velocity magnitude). Direction and rate of the motion are represented by the hue and saturation of different colors, respectively (Baker et al., 2011). For instance, the two blue/purple color-saturated areas at the plume front represent fast-rising bomb "swarms" exiting the plume, green and yellow zones at the plume side denote diverging ash-bombs fallout areas, and orange to purple zones at the plume head mark large-scale vortex motion. Arrows also display the direction and the velocity of the plume, subsampled every 16 pixels. Note the artifact propagation of the flow field away from the plume area.

achieved using the FLIR ThermaCam software, taking into account the temperature and the humidity of the atmosphere and the distance from the camera to the plume. We did not correct for other effects such as sunlight intensity, angle of view, emissivity of the source, and absorption of radiations due to gas and aerosols (Sawyer & Burton, 2006; Spampinato et al., 2011; Harris, 2013), and thus, only relative, not absolute, values of temperature are reported in this study. From the original data set of more than 200 videos, quantitative parameterization was performed on 43 (24 thermal, 12 high-speed, and 7 SONY) selected videos covering 29 explosions with the best visibility (Table 1).

3.2. Plume Parameterization

3.2.1. Plume Motion

In order to track the motion of the plumes, we manually tracked the top part of individual vortexes, which represent clearly visible features, shifting to a new vortex when the tracked one started blurring with the plume. This method allows tracking the motion of the plume in all its different regions, although for most purposes we just refer to the front velocity, that is, the velocity of the uppermost part of the plume. Manual tracking was performed using the MtrackJ plug-in of the ImageJ software (Abramoff et al., 2004).

To highlight individual structures (e.g., vortexes and bombs) and to detail the velocity field of the plume at specific development stages, we used the optical flow computer vision technique that compare to the widely used particle image velocimetry technique and allowed a characterization of the flow. Following brightness constancy assumption over the measurement time, this method solves the optical flow equation based on pixel intensity (Baker et al., 2011). Couples of frames at 10 frame intervals were selected from the thermal videos and preprocessed by extracting the thermal gradient of each frame combined with a temperature threshold visually adjusted for each explosion in order to remove the background (Figures 2a and 2b). Then we used the optical flow MATLAB toolbox (Sun et al., 2010, 2014) to extract the direction and rate of plume motion in between these two frames using the "classic + nl-fast" method (Figure 2c). Velocity estimations from manual tracking and optical flow diverge by less than 4%. The results of the optical flow analysis are displayed using color encoding of flow vectors (Baker et al., 2011).

In all cases, the reported velocities are two dimensional, not accounting for motion toward or away from the camera. Considering the tilt angle of the camera at each location and the height reached by the plumes, our measurements may, in the case of a plume rising vertically, underestimate plume velocity by less than 10%, 22%, and 25% for Stromboli, Fuego, and Sakurajima, respectively (Figure S1 in the supporting information).

Deviations from the vertical in the rise direction of the plumes, due to local wind and oblique ejection at the vent, are not accounted for in our analysis.

3.2.2. Plume Volume Over Time

The evolution of plume volume over time was estimated by manually contouring the plume area at a regular frame interval, individually defined for each video. Plume area was then converted into volume, assuming the plume to be axisymmetric (Valade et al., 2014). The plume is divided into horizontal slices, each one having volume equal to that of a cylinder one pixel in height and with the diameter corresponding to the width of the plume at that height. The sum of the volume of all slices provides an estimate of plume volume at any frame (Valade et al., 2014). Applying this method over several frames gives an estimation of the evolution of plume volume over time. Repeated measurements on the same explosion from different cameras located at the same place deviate by about 10% on average. Uncertainties due to the axisymmetric plume assumption have been quantified on two explosions at Stromboli volcano using two cameras at different location with an angle of 90° between them and the plume and are about 46% (Figure S2 in the supporting information).

3.2.3. Ash Eruption Rate

An estimation of the ash mass in the plume as fraction of the total erupted mass, or ash eruption rate (AER), is provided following the principles described in Morton et al. (1956) and Yamamoto et al. (2008). This estimation concerns only the solid fraction of the buoyant plume, which, on the timescale of our observation, is coupled with the gas, while the mass of larger clasts and gas is not taken into account. Based on our calculations in order to obtain a Stokes number of 1 in the case of our transient plumes, the average particle diameter would range between 1.8 and 13 mm. Consequently, the solid fraction coupled with gas in our case includes only ash particles (i.e., smaller than 2 mm). To apply this method, we selected explosions that fulfilled the following two criteria: (1) having a fully buoyant phase while the plume is still entirely in the field of view of the cameras and (2) having a well-defined gas-thrust phase. In this study, the plume is assumed fully buoyant when its front velocity is not decreasing anymore with time. As an additional, conservative precaution, we also considered only rise velocities lower than 15 m/s, as used by Patrick (2007).

AER calculation requires the estimation of the concentration of ash C_{Ash0} and the volumetric flux at the vent. C_{Ash0} is derived from observation of the buoyant phase of the plume rise. In this phase, the vertical front velocity is determined by the plume buoyancy and can be linked to the plume density ρ_P at a given time (Morton et al., 1956; Yamamoto et al., 2008):

$$\rho_P = \rho_a - \frac{3W^2}{zg}\,\rho_a \tag{1}$$

with ρ_P corresponding to plume density (kg/m^3), ρ_a being atmosphere density at the considered elevation (kg/m^3), W is the front velocity (m/s), z is the height of the plume front above the vent (m), and g is the acceleration due to gravity (m/s^2). This plume density is estimated at a given time t_b selected for each explosion and corresponding to a stage of front velocity trend stable and below 15 m/s. Assuming that the volumetric fraction of gas in the plume is close to 1 and that $\rho_P - \rho_{\mathrm{gas}}$ is constant in the plume, we obtain the following equation (Yamamoto et al., 2008):

$$m_{\mathrm{ash}} = \left(\rho_P - \rho_{\mathrm{gas}}\right)V \tag{2}$$

with V corresponding to the estimated plume volume and ρ_{gas} corresponding to the average density of gas present in the plume.

In this method, we estimate ρ_{gas} at a late development stage where plume rise buoyantly. Consequently, the gas present in the plume mainly results from entrainment of surrounding atmosphere, and thus, we chose to assume the density of the gas equivalent to the density of the atmosphere at the temperature of the plume head:

$$\rho_{\mathrm{gas}} = \rho_{\mathrm{atm0}}\frac{273.15}{T_{\mathrm{head}}}, \tag{3}$$

where ρ_{atm0} is the atmosphere density at 273.15 K. However, since we do not know the proportions of air and volcanic gases present in the plume over time, we performed a second estimation corresponding to the intermediate value between two end-members of volcanic gas mixtures at Stromboli volcano, the first including

64% H_2O, 33% CO_2, and 3% SO_2 and the second with 80% H_2O, 17% CO_2, and 3% SO_2 (Aiuppa et al., 2010; Burton et al., 2007). Using volcanic gases instead of atmosphere decreases the gas density by about 11%.

Thus, we obtain m_{ash}, which represents the total mass of ash present in the plume, as measured during its buoyant phase. Starting with m_{ash} and assuming it to be equal to the total mass of ash erupted during the explosion, we can then retrieve the concentration of ash at the vent during the gas-thrust phase, by using our high-speed measurements of exit velocity. In fact, if we suppose that it remains constant with time, C_{Ash0} is obtained by dividing m_{ash} by the volume of the ash-gas mixture erupted at the vent (V_0):

$$C_{Ash0} = \frac{m_{ash}}{V_0}. \tag{4}$$

The assumption of ash concentration constancy over time at the vent is commonly used in literature due to a lack of constrains on this parameter. This is particularly true for analogue experiments and numerical simulations where usually the ejected flow keeps the same properties all along the ejection phase (e.g., Chojnicki et al., 2014; Clarke et al., 2002). Assuming the vent diameter to be constant over time, V_0 can be retrieved using the exit velocity (v_{exit}) of the gas-ash mixture at the vent and the estimate of the vent surface (S):

$$V_0 = \int_{t0}^{tf} v_{exit} S \, dt \tag{5}$$

with t_0 and t_f corresponding to the beginning and the end of the ejection phase, respectively.

Finally, under the assumption that C_{Ash0} can be considered constant over time, the instantaneous AER (kg/s) is obtained by

$$AER = v_{exit}.S.C_{Ash0,} \tag{6}$$

which can be simplified in this case in

$$AER = m_{ash} \frac{v_{exit}}{\int_{t0}^{tf} v_{exit} \, dt}. \tag{7}$$

Note that this last simplification provides an AER equation, which is independent from vent diameter.

Exit velocity at the vent is thus a crucial parameter for AER estimates, but it cannot be directly measured in our (and most other) case, because (i) the vent is not always in direct view of the cameras and (ii) we can only observe the exterior of the plume, where the velocity is lower than that at the centerline. In our case, we can only measure the ejection velocity of the plume (vo) at its surface and as near as possible to the vent with a 0.4, 0.67, and 1.45 m maximum resolution for Stromboli, Fuego, and Sakurajima, respectively. However, here the velocity of interest is the ejection velocity at the vent and on its axis (v_{exit}). Turner (1962) experimentally showed in the case of a steady state plume that the front velocity (vf) corresponds to 0.6 times the mean velocity on the centerline (vc) of the plume at the same height. To apply this relation to our transient plumes, we considered only the period 0.5–1 s after the beginning of explosions, using our front velocity data collected to infer the centerline velocity of the plume at that location. Here we make the assumption that exit velocity is homogeneous over the whole vent section.

$$vf = 0.6vc. \tag{8}$$

This result is then compared to vo and a correction factor (b) is obtained.

$$b = \frac{vc}{vo} \tag{9}$$

b is then applied to vo for the whole gas-thrust phase duration.

v_{exit} is equal to vc only below a distance above the vent equivalent to about 5 to 12 vent diameters in the case of turbulent, round jets and then decreases for greater distances (Abdel-Rahman et al., 1997; Bogusławski & Popiel, 1979; Freund et al., 2000; Hussein et al., 1994; Iqbal & Thomas, 2007; Panchapakesan & Lumley, 1993; Quinn, 2006; Xu & Antonia, 2002). To ensure our cases fell into this 5 to 12 vent diameter cases, we estimated vent size and depth. For Stromboli we used vent diameter estimations from Chouet et al. (1974) and Gaudin et al. (2014) (2–3 m). For Sakurajima and Fuego we used estimations obtained tracking the trajectory of about 50 bomb-sized pyroclasts. These trajectories were then fitted with parabolic functions and prolonged inside the vent to estimate vent diameter and depth from the location and width of their crossing area

(cf. Dürig et al., 2015). For our case, the velocity measurements we performed at the base of the plume are always below or around seven vent diameters from the source and thus representative of exit velocity after centerline correction. Vent shape can also play a role in the exit velocity evolution (Cigala et al., 2017). Such variation would fall within the measurement error and thus is not taken into account here.

The error propagation has been taken into account by calculating the mathematical uncertainty at each steps of the method. The associated error ranges between 40 and 154% of the calculated AER. Variations of this value are due to the relative error associated to each parameter involved in the calculation.

4. Results

4.1. Plume Morphology and Evolution

All observed events display an initial gas-thrust phase at the vent and a subsequent, slower rise of the ash-loaded plume (Figure 3) in agreement with previous observations (Marchetti et al., 2009; Patrick, 2007; Patrick et al., 2007).

The initial jet-like emission often has a spearhead morphology in the first few seconds and is always accompanied by the ejection of bomb-sized pyroclasts, occasionally simultaneously from multiple vents and at velocities up to hundreds of meters per second (supporting information Movie S7 explosion Fu_4 and Movies S1 and S2 explosion Sa_1). The initial jets evolve into a slower rising structure through the development of vortexes at different scales, often combined and /or dominated by the formation of a large, toroidal, ring (or head) vortex (Figure 4). In the simplest case, one main vortex involves the largest part of the plume with a cylindrical body connecting it to the vent (e.g., supporting information Movie S4 explosion Sa_10). The rotation of this vortex involves absolute velocities in the order of tens of meters per second, in a flow field that is upward divergent at the summit and downward convergent at its base, below which displacement vectors point to a strong motion toward the vortex interior. In the cylindrical body velocity is slower, with motion toward plume interior also visible. In some cases, a pinch-off is observable (Peña Fernández & Sesterhenn, 2017), corresponding to successive ring vortexes formation, the new ones still developing while the previous ones start to detach from the plume through a neck, as experimentally observed by Chojnicki et al. (2014) (supporting information Movie S7, explosion Fu_4). In other cases, a first plume is developing before a second ejection phase, occurring with a different angle or from a different vent, which generates a secondary structure and impact the overall plume development (Figure 4 Sa_8, Figure 3, and supporting information Movie S3, explosion Sa_8).

The time evolution of plumes and respective source activities are best documented by changes in their apparent temperature. This was measured along a vertical profile located along the plume axis to track plume's rise and cooling and along a horizontal profile located just above the vent to track changes in the activity and location of vents (Figure 2a). The temperature along these profiles is then plotted against time to provide a characteristic diagram (Figure 5). Finally, the integration of values of the horizontal profiles is plotted over time to qualitatively illustrate the discharge history at the vent for each corresponding plume.

Vertical changes highlight well the rise of the plume front, which often displays a sharp kink between two different rise velocities (Figure 5). The decrease with height of the apparent temperature of the plume surface is noticeable both at the plume front and in lower regions. Bombs appear as parabolic traces. Individual ejection pulses and vortexes are visible both in the vertical and horizontal evolution plots. Pulses inject new, hot material with a clear thermal signature visible close to the plume base. Vortexes cause hotter, inner parts of the plume to be first exposed at the surface and then cooled by conduction and convection, resulting in feather-like thermal features (Figure 5). Horizontal temperature evolution at the vent effectively traces lateral variations in the ejection source, which shifts position both sharply, and gradually, as the result of vent shifting and/or changes in the ejection angle of the gas-pyroclasts mixture. Finally, integrated horizontal temperature evolution at the vent reveals in most cases an asymmetric temperature anomaly, assumed to be somehow representative of the discharge history, with a short waxing phase, a peak—or plateau, and a longer waning phase. More than one peak phase may occur (e.g., St_12), and occasionally (e.g., Sa_10), an almost steady state supply seems to cover the whole duration of our videos.

The initial development of the observed plumes is essentially controlled by the source dynamics: occurrence of multiple ejection pulses, their number, intensity, duration, separation in time, and source

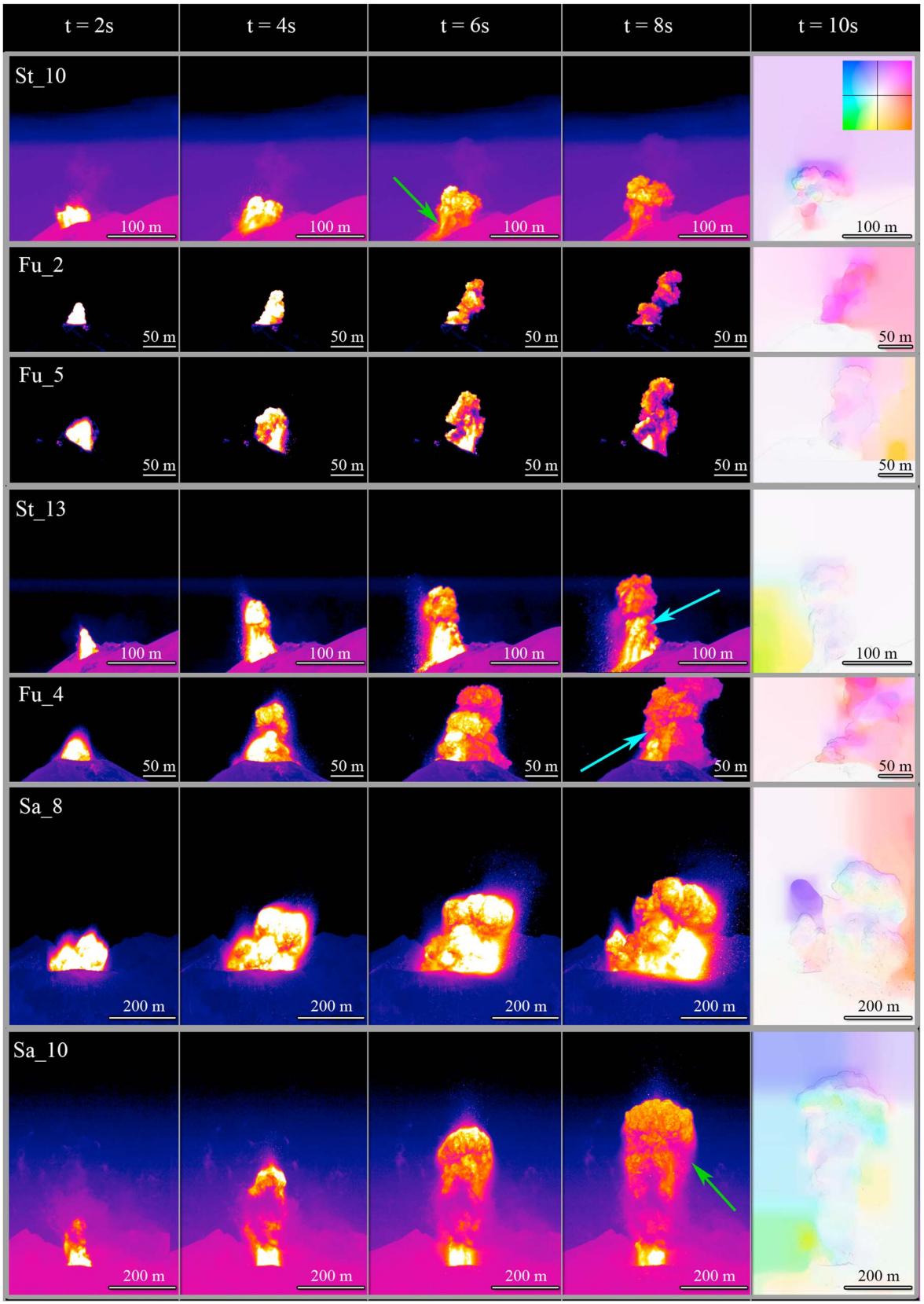

Figure 3. Still thermal frames showing the initial development of plumes from seven explosions. In the right-hand column, the velocity field of the plume after 10 s. Velocity and temperature color scales differ from case to case. Green and blue arrows correspond to ash downdrafts and helical motion of the plume, respectively.

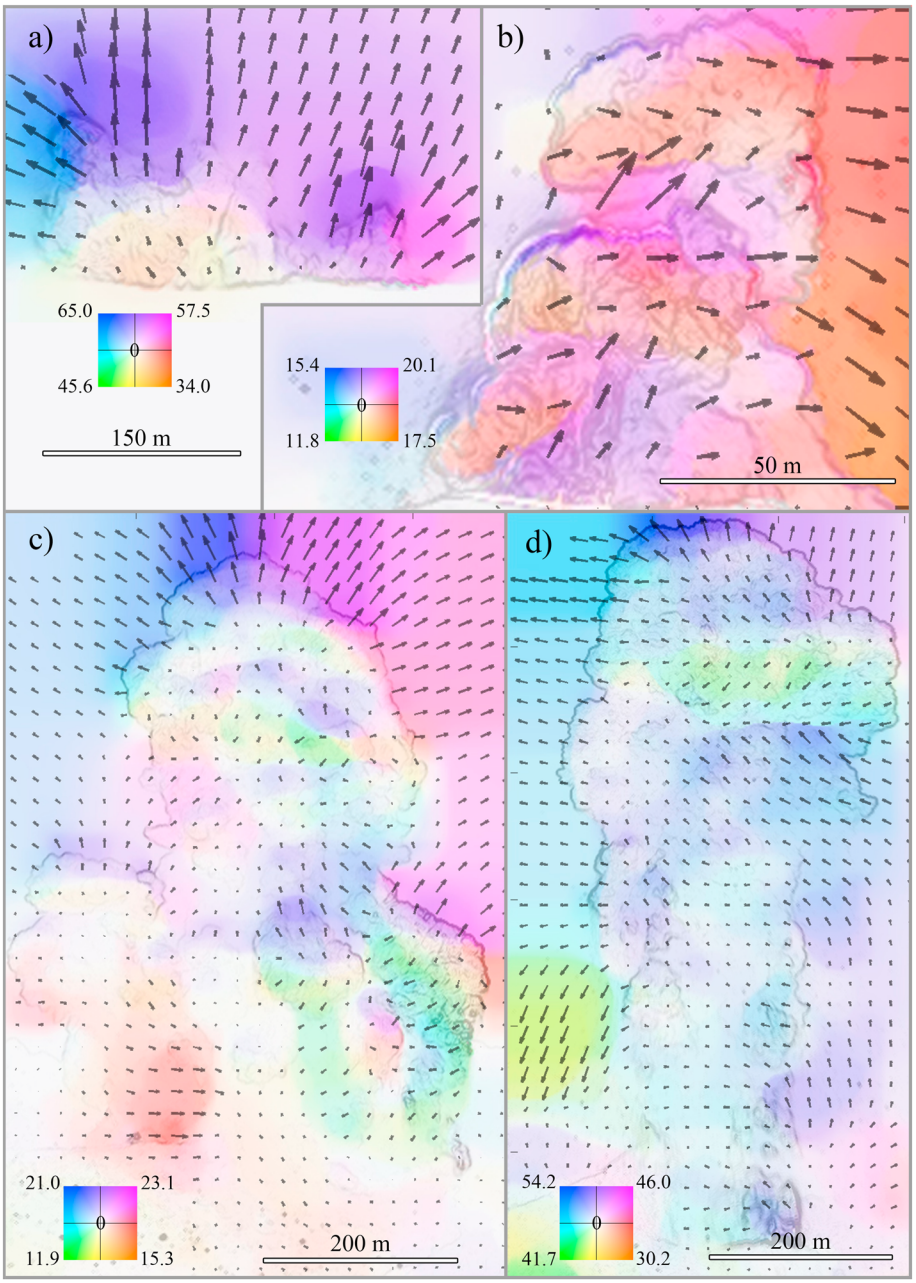

Figure 4. Flow field of volcanic plumes from the (a) Sa_1, (b) Fu_4, (c) Sa_8, and (d) Sa_10 explosions at 1.8, 4.5, 22.5, and 15.4 s after their beginning, respectively. Plume motion is displayed both using the color scale and subsampled arrows. Sa_1 features two jets with different angles from one or two different vents. Velocity is maximum (up to 65 m/s) at each jet front due to the ejection of bombs and ash in a radial pattern that heralds the formation of a ring vortex. Downward motion at the base of the jet on the left possibly marks the beginning of air entrainment. Fu_4 shows two similar, successive ring vortexes (marked by divergent velocity fields) and with upward air influx at their base (most developed for the upper one). Crosswind moves the entire plume from left to right, visible in the lack of leftward oriented (blue to green) velocity vectors. Sa_8 displays a complex plume formed by multiple ejection pulses from different vents. Several ring vortexes are present, marked by horizontal transitions of the flow field from upward- to downward-dominated motion. The uppermost and largest structure at the plume head displays two/three of these transitions, revealing several merging ring vortexes. Sa_10, a plume almost sustained by multiple, fast-repeating pulses from the same vent, displays a large ring vortex, capped by overrunning bombs (high vertical velocities at plume's head) and followed by a strong (approximately 20 m/s) area of air entrainment at the summit of a cylindrical body. Within the body, rising vortexes appear on the right-hand side (purple-bluish areas) and combine with a leftward oriented crosswind component.

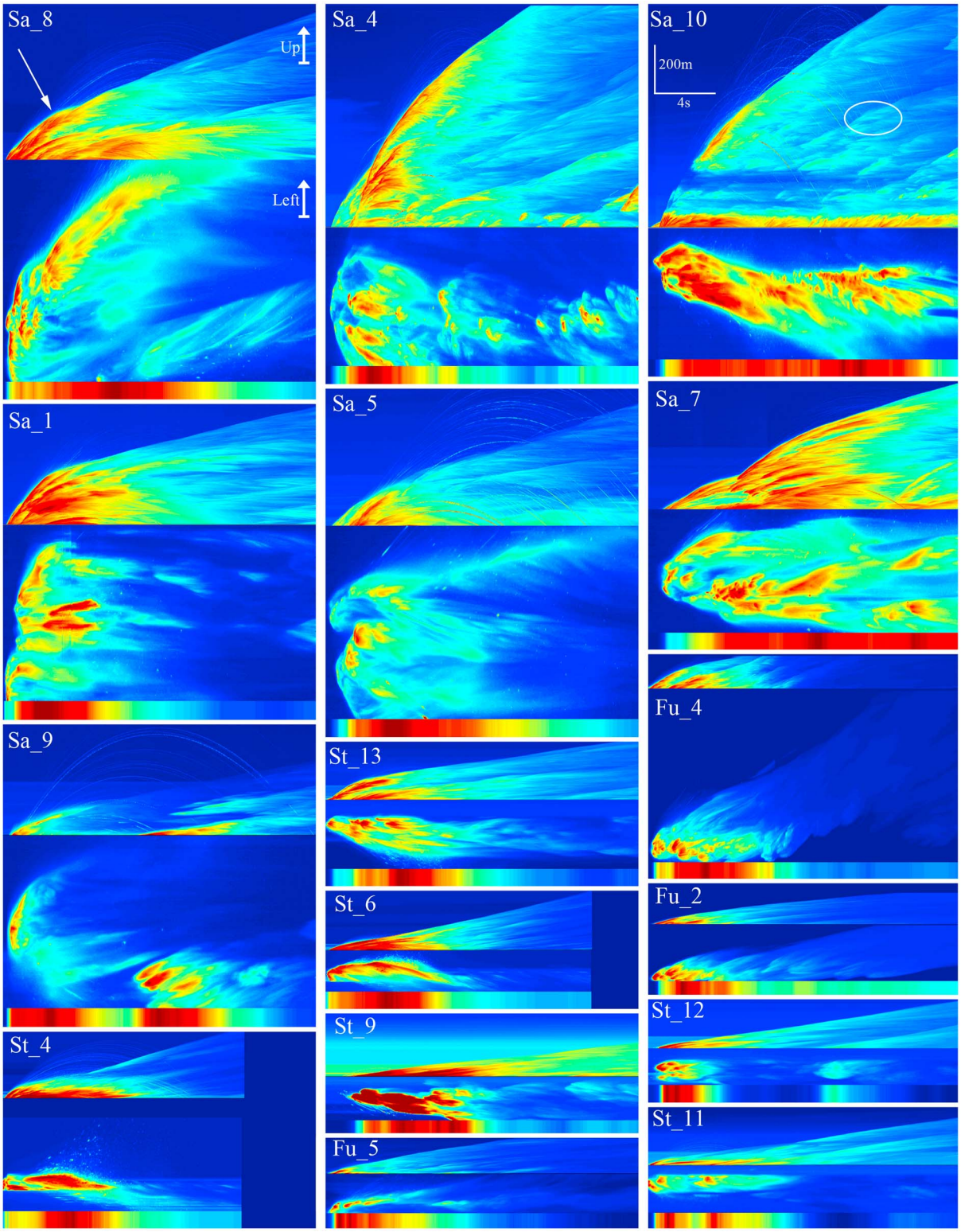

Figure 5. Vertical (top), horizontal (middle), and integrated (the average of horizontal values at any time, bottom) evolution of apparent plume surface temperature over the first 20 s of representative explosions (see Figure 2 and section 3.2.1 for method description). Explosions are sorted downward in decreasing order of ejection duration and rightward in decreasing lateral span of ejection source. Vertical evolution tracks the rise and cooling of plume front (arrow in Sa_8 mark the kink in plume front rise velocity) and vortexes (circle in Sa_10), as well as the trajectory of ballistic projectiles (Sa_5). Horizontal evolution illustrates well the number and duration of ejection pulses and their lateral variability. Integrated evolution is a proxy for the discharge history of each explosion. Space and timescales are the same for all explosions, while the apparent temperature scales (not shown) are normalized for each case.

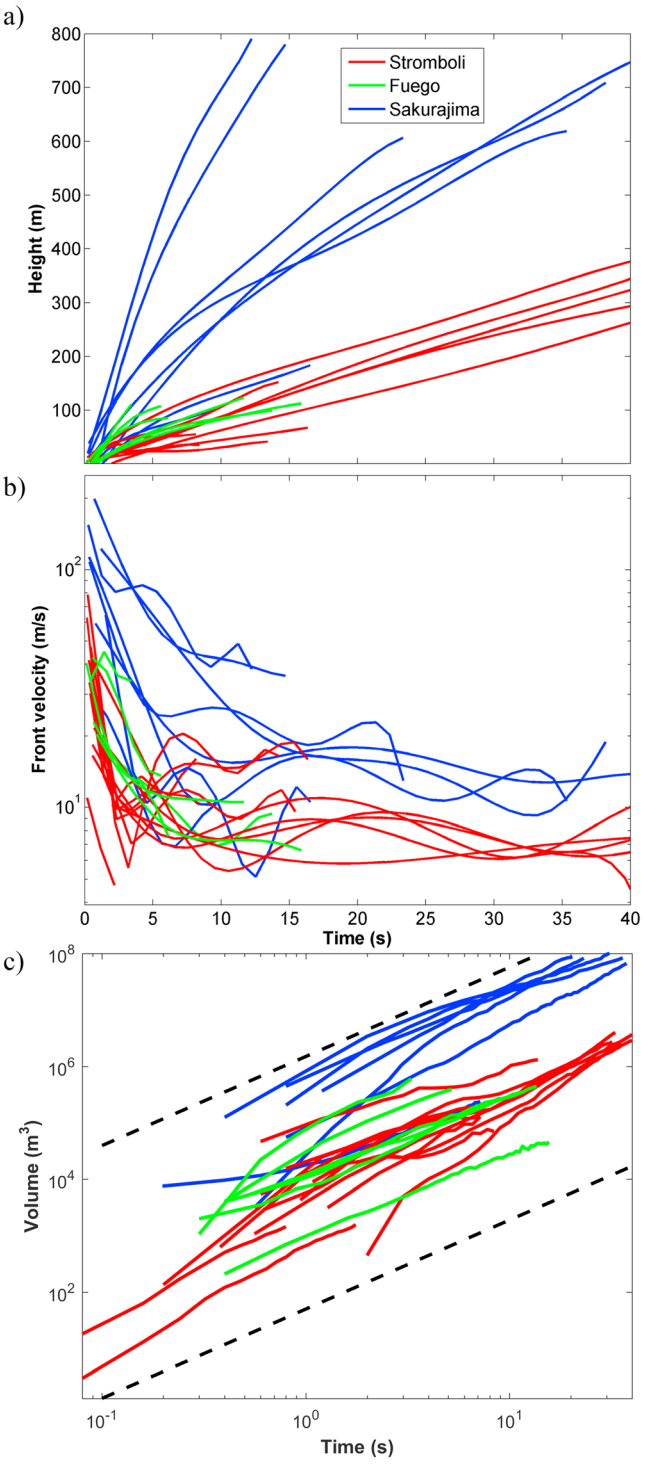

Figure 6. Evolution of (a) plume height, (b) front velocity, and (c) volume measured until the time when the plume front exited the camera's FOV. For a better visualization, velocity curves were smoothed by a fourth-order polynomial fit (cf. Patrick et al., 2007). The black dashed lines in Figure 6c bound the observed interval and have a slope corresponding to the average volume increase rate for all measured plumes. The corresponding average power law coefficient is 1.58.

vent (Figures 3–5). The jets and vortexes originated by these pulses interact and combine, giving rise to a wide spectrum of plumes morphologies and evolutions. Simple thermals are never present in our records; the shortest emission (St_10) still features a few ring vortexes from more than one ejection pulse. If ejection pulses are large and spaced by long time intervals, they may form multiple, distinguishable ring vortexes (e.g., Fu_4). Conversely, overlapping ejection pulses from one or a few close-by vents, if prolonged over tens of seconds, result in plumes with a large ring vortex at the head and a cylindrical body with smaller rising vortexes (e.g., Sa_10). These plumes are, among our cases, those whose morphology is closer to that of a sustained eruption column. Explosions involving ejection pulses with variable timing (from overlapping to a few seconds) and multiple vents (up to more than 100 m apart) produce complex plume morphologies, characterized by several independent large structures with merging and overlapping vortexes and jets (e.g., Sa_8).

Beside ejection pulses, other observed controls on plume morphology include (1) crosswinds, affecting the interaction between jets from subsequent ejection pulses by laterally shifting the developing plume before initiation of secondary jets, like in the wind-bent plumes with well-separated vortexes of the Fuego cases (Figure 3 and supporting information Movies S5 and S6, explosion Fu_1); (2) the occurrence of "swarms" of bomb-sized pyroclasts, dragging the ash, piercing the head of the plume from its front while rising and causing ash downdrafts at the plume margin while falling (Figure 3); and (3) partial collapses of the densest part of the plume to form small pyroclastic density currents, as observed at Fuego and Sakurajima volcanoes (Figure 4 and Fu_4). Finally, we also report ash downdrafts developing from the lower corner of ring vortexes and the wind affected outer part of the plume rotating in helical motion (Figure 3, green and blue arrows, respectively) (Patrick, 2007).

Despite obvious differences in the intensity (index of eruption rate) and magnitude (index of erupted mass) of the activity at the three studied volcanoes, the above mentioned qualitative relationships between source variability and plume morphology hold true and no clear boundary divides them for plume morphology or evolution.

4.2. Plume Parameterization

4.2.1. Rise Velocity and Volume

Depending on the magnitude of the event, plume heads reach heights between 100 and 800 m within 40 s after ejection (Figure 6). Maximum plume rise velocities, always attained at explosion onset, are 113, 70, and 227 m/s, while average buoyant rise velocities are about 9, 10, and 13 m/s at Stromboli, Fuego, and Sakurajima, respectively. Rise velocity of the plume head reflects the two phases previously described on the basis of the plume morphology. During the gas-thrust phase, the rise velocity falls rapidly, due to the dissipation of the momentum, while during the buoyancy phase, the rise velocity remains fairly stable, with marked oscillations and in some cases late stage increases in rise velocity (e.g., Sa_1, St_10, and St_13). The transition between the two velocity phases is often abrupt and occurs 2 to 15 s after the beginning of the explosion. Late stage velocity increases are less obvious at Fuego volcano, possibly because the field of view is small with respect to plume rise (Figure 6). The transition between the two rise velocity

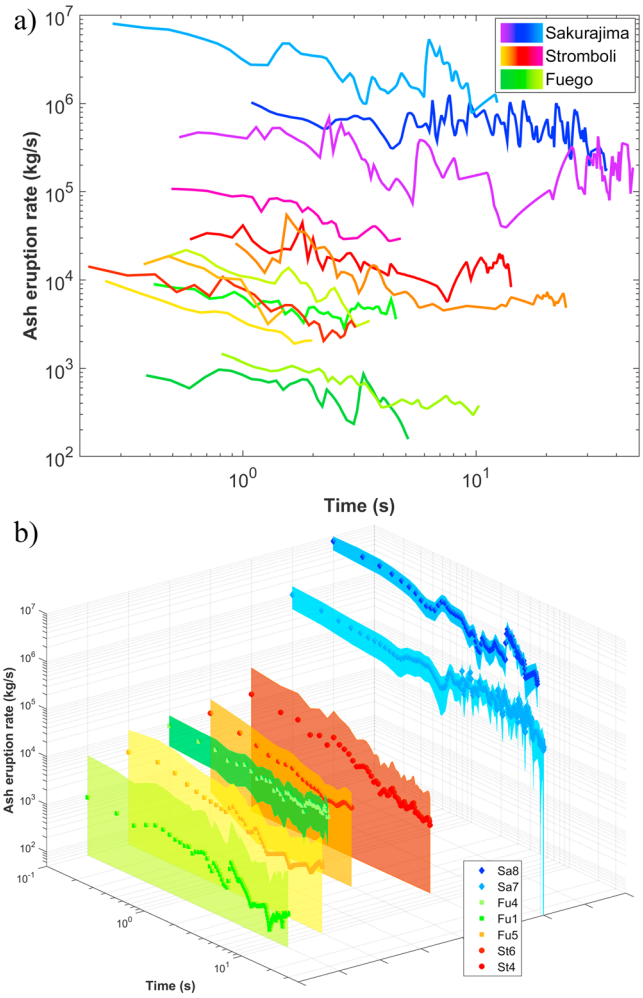

Figure 7. Ash eruption rate evolution over time, (a) for all processed videos and (b) for selected explosions with their associated error (colored area). Note logarithmic axes scale.

phases is strongly influenced by the number, duration, and time interval of ejection pulses that feed the plume: shorter, less, and closer pulses result in earlier and more abrupt transitions, as exemplified by the Stromboli case (Figures 5 and 6). On the contrary, at Sakurajima, longer-lasting ejection phases result in a slower decay of velocity in the first phase and a smoother transition to the second one. Fuego cases are in between these two. The velocity of individual vortexes trailing behind the plume head, as measured by manual tracking and optical flow, ranges 5–22 m/s and decreases over time.

Within our limited time observation windows, plumes attain volumes ranging from about 4.2×10^4 to 1.2×10^8 m^3. In most cases, volume grows as a power law function of time with the Sakurajima explosions showing the largest volumes, and growth rates. Despite the very different initial and final volume attained by the plumes, all plumes display a similar expansion rate, as expressed by the power law coefficient, which shows an average value of 1.58 and ranges between 0.72 and 2.62. The average coefficient per volcano is 1.64, 1.47, and 1.56 for Stromboli, Fuego, and Sakurajima, respectively. Higher coefficients, from 1.69 to 2.62, pertain to explosions with longer and more sustained ejection pulses such as Sa_4, Sa_7, Sa_10, St_9, and Fu_6, while events with shorter and more spaced pulses and wind and bombs interactions, such as Fu_1, St_4, St_7, and St_8, display lower coefficient in between 0.72 and 1.26.

Both velocity and volume results show a clear overlap of data in between Stromboli and Fuego cases, while most of Sakurajima's events appears to be larger and with higher rise velocities.

4.2.2. Ash Eruption Rate

Estimation of ash eruption rate and its evolution over time was performed for six Stromboli, four Fuego, and three Sakurajima explosions (Figure 7 and Table 2), corresponding to the best cases from our data set with respect to AER method requirements. Results show that the selected events cover a wide range of eruption intensities and magnitudes. Fuego and Stromboli display similar time-averaged AER values, in the order of 10^2–10^4 kg/s, while Sakurajima cases are about 2 orders of magnitude higher, with time-averaged AER of about 10^5–10^6 kg/s. Using the average ash eruption rate and the ejection duration (estimated based on the videos), a cumulative erupted ash mass is obtained. Stromboli and Fuego cases, with similar AERs, eject 10^3–10^5 kg of ash in a few seconds, while the larger magnitude and more intense Sakurajima cases eject up to 10^7 kg of ash in up to 40 s (Table 2). In most cases, the time-resolved AER peaks at the beginning of the explosion, with subsequent increases occasionally being related to later ejection pulses. The initial AER peak, lasting about 1 s, can be up to 2 orders of magnitude higher than the final one and up to 1 order of magnitude higher than the time-averaged one.

5. Discussion

Even though Vulcanian and Strombolian eruptive styles may differ in several aspects (Clarke et al., 2015; Taddeucci et al., 2015), our results show that initial plume dynamics from both styles share many common features. In both cases the impulsive, unsteady nature of the eruption mechanism strongly controls the features and evolution of the resulting transient plumes.

5.1. Diversity of Plume Morphology and Evolution

Considering two theoretical end-members of plume morphology, that is, impulsively released thermals and steady state plumes, the transient ones we describe fall in a broad, intermediate range. Some general features in morphology evolution are recognizable in almost every case. All explosions are characterized by the

Table 2
Summary of Ash Eruption Rate (AER) Results and Parameters

Explosion	ρ^*_{Plume} (kg/m^3)	ρ^*_{Atm} (kg/m^3)	AER average (kg/s)	AER average error (%)	Cumulative ash mass (kg)	Ejection duration (s)	t_b (s)	v_{exit} correction factor	v_{front} buoyancy (m/s)	v_{front} max (m/s)	$v_{centerline}$ (m/s)	v_{exit} max (m/s)
Sa_5	1.195	1.117	1.85E+05	140	8.69E+06	46.94	33	1.0	13.4	72.5	120.8	116.5
Sa_7	1.237	0.836	6.63E+05	55	2.40E+07	36.12	33	1.3	10.0	54.2	90.3	70.6
Sa_8	1.267	0.910	2.87E+06	40	3.52E+07	12.28	23	1.6	6.4	131.2	218.7	138.7
St_4	0.881	0.855	2.47E+04	69	7.43E+04	3.01	10	1.7	11.6	111.5	185.8	111.5
St_5	1.138	1.083	9.73E+03	143	7.54E+03	1.52	13	1.7	7.3	56.0	93.3	54.3
St_6	0.593	0.540	7.76E+03	61	1.51E+04	1.95	6	1.4	13.4	46.0	76.7	57.0
St_10	1.236	1.165	5.25E+04	137	2.94E+05	5.6	30	1.5	6.3	21.3	35.5	23.5
St_12	1.235	1.138	1.48E+04	144	2.51E+05	17	33	1.3	6.3	19.6	32.6	26.1
St_13	1.190	1.093	7.42E+03	124	1.87E+05	25.16	25	1.5	8.5	59.1	98.5	65.0
Fu_1	1.096	1.083	4.86E+03	150	2.48E+04	5.09	10	1.0	7.7	24.7	41.2	47.2
Fu_2	1.253	1.135	5.36E+02	142	6.13E+03	11.43	14	1.7	3.7	26.8	44.7	26.6
Fu_4	0.939	0.777	7.55E+03	56	3.54E+04	4.69	6	1.5	11.6	49.4	82.3	55.4
Fu_5	1.016	0.949	5.33E+03	154	1.73E+04	3.25	8	1.0	4.5	24.8	41.4	43.5

Note. Plume and entrained air densities are marked as ρ^*_{Plume} and ρ^*_{Atm}, respectively, and measured at the time t_b. ρ^*_{Atm} has been calculated using equation (3) based on plume head temperature at t_b. The cumulative ash mass corresponds to the integration of the average AER over the whole ejection duration. The v_{exit} correction factor is the correction applied to measured plume base velocities in order to retrieve exit velocities at the vent. The v_{front} buoyancy corresponds to the front velocity of the plume at t_b. The v_{front} max corresponds to the maximum front velocity measured on the plume. The $v_{centerline}$ is the calculated theoretical velocity at the plume centerline following Turner (1962). The v_{exit} max corresponds to the maximum velocity manually measured at the plume base.

presence of a spearhead jet that evolves in a ring vortex and then often transits in a more complex morphology during the buoyant phase, as already described in literature (Delle Donne & Ripepe, 2012; Patrick, 2007; Patrick et al., 2007; Webb et al., 2014; Zanon et al., 2009) and as experimentally shown by Kitamura and Sumita (2011). Complex plume morphologies originate from the occurrence of multiple ejection pulses, as visible in the thermal signature and velocity measurements (Figures 3 and 4), from one or more vents.

The morphology of transient plumes from unsteady sources has been investigated experimentally by Chojnicki et al. (2014), which injected finite volumes of water into water at constant temperature to get neutrally buoyant jets, following a" Gaussian-shaped history of flux over time." To visualize the flow field, a mixture of 10 μm diameter glass spherical particles was added to the jet and the recipient. The resulting experimental plumes varied in morphology over time along this Gaussian history: at the beginning, during the increase of momentum flux, a jet forms and then evolves into a rounded head, or ring vortex, followed by a cylindrical tail; during the decrease phase, after the peak flux, the ring vortex starts to overrun the body of the plume and a narrow neck forms in between. Finally, after the end of flux momentum, the body of the plume develops a new ring vortex at the head and a conical tail, both enlarging linearly while rising.

Comparing our observations with the experimental results of Chojnicki et al. (2014), we note that there is a general convergence of morphological features, but our study cases invariably display a higher degree of complexity, both in the variety of morphologies observed and in their evolution over time. The general convergence of features suggests that momentum is the dominating force of plume morphology in our observations of initial development, because buoyancy is entirely absent in the experiments of Chojnicki et al. (2014). Buoyancy, while leaving a clear mark in the velocity trend of the plume head (Figure 6), does not significantly affect plume morphology in the region close to the vent, which is the focus of our observations.

Besides the obvious differences between nature and a controlled laboratory environment, two main factors explain the increased complexity of our observations. First, our estimates of ejection velocity, discharge history, and ash eruption rates (Figures 5 and 7) disagree with a Gaussian-shaped history of ejection flux at the vent, showing a maximum velocity at the very beginning of the ejection pulse, as already observed in several other cases (Gaudin et al., 2014; Ripepe et al., 1993; Taddeucci et al., 2012). This observation does not imply the absence of an acceleration phase at the beginning of the gas-thrust phase. A short acceleration exists but is not observed here due to geometrical constrains. Second and most relevant, almost all our explosions featured not one but multiple ejection pulses, also from more than one vent (Capponi et al., 2016; Gaudin et al., 2014; Scharff et al., 2015; Taddeucci et al., 2012). Our observations focus on the initial development of plumes

in a region, which is relatively close to the vent area, and it remains open to discussion how much of the complexity we observe is preserved in the morphology of plumes at later moments and higher elevations above the vent.

Of the several other factors influencing plume evolution, some have received more attention, like the presence of crosswind (Bonadonna et al., 2015) or the occurrence of partial collapses (Neri et al., 2003). Here we want to highlight that our observations suggest that large bomb "swarms," both while descending and rising, can impact ash particles dynamics within the plume and cause premature ash falls.

Interestingly, we do not observe any clear difference of plume morphology and its evolution, even considering plumes with more than 1 order of magnitude differences in size and resulting from activity styles from Strombolian to Vulcanian. It appears that all those volcanic plumes belong to a continuous spectrum of eruption styles as first suggested by Wilson et al. (1978).

5.2. Plume Parameterization

5.2.1. Velocity and Volume

A twofold trend characterizes the rise velocity of the front of most of the observed plumes (Figure 5), that is, first a sharp drop and then oscillations around a constant value. This trend has been observed frequently for transient volcanic plumes, and its two parts have been interpreted as the phases when gas-thrust and buoyancy drive the plume, respectively (Blackburn et al., 1976; Chojnicki et al., 2015a; Johnson, Harris, et al., 2004; Marchetti et al., 2009; Patrick, 2007; Patrick et al., 2007; Sahetapy-Engel & Harris, 2009). Front velocity fluctuations linked to multiple ejection pulses superimpose on the general trend, occasionally as sharp velocity changes but more often as smooth deviations from the trend.

Initial front velocities measured at Stromboli, Fuego, and Sakurajima, respectively, range from 14 to 113 m/s, 21 to 70 m/s, and 32 to 227 m/s at the very beginning of the explosion and values of average buoyant velocity converge to 9–13 m/s. Overall, the results match the one of Patrick (2007) and Patrick et al. (2007) for initial front velocities at Stromboli volcano, ranging from 10 to 50 m/s and maximum buoyant rise of 10.9 m/s. As for the explosions closer to Vulcanian style, Webb et al. (2014) report initial front velocities between 6 and 60 m/s at Colima volcano (Mexico), De Angelis et al. (2016) measured a buoyant velocity of about 10 m/s at Santiaguito volcano (Guatemala), and Suwa et al. (2014) report initial rise velocities of about 34 m/s at Sakurajima. Their estimation of the velocity of trailing vortexes also matches well our measurements.

At Sakurajima, our estimated centerline exit velocities are maximum (90–292 m/s) in the first seconds of ejection and later on average in the range of 39–121 m/s. These values are comparable with those estimated by Suwa et al. (2014) (40–50 m/s) in the same time interval. At Stromboli, maximum centerline values (76–186 m/s) are lower than maximum literature exit velocities (up to 400 m/s, Taddeucci et al., 2012), which, however, were measured in ash-free explosions. Importantly, our data set enabled comparison of the front velocity of the same plume as measured with different camera setups. As expected, higher frame rate and higher magnifications results in higher measured velocities for the same plume, up to 50%.

Volumetric data show that plumes from Stromboli, Fuego, and Sakurajima, follow a power law trend in their time evolution (Figure 6):

$$V = Ct^{\alpha}, \tag{10}$$

with t the time, C the proportionality coefficient, and α the power coefficient. Theoretically, the radius of a thermal grows with the square root of time resulting in a time-volume power law dependency with slope 1.5 (Turner, 1979). This value is remarkably similar to the 1.58 α average value of our plumes, which suggests that the air entrainment mechanism in our cases is similar to the one of individual thermals. However, our results also show that this coefficient deviates from the average value as a result of plume source properties, more "sustained" conditions (i.e., more prolonged and closer in time ejection pulses) showing higher values, potentially reflecting the additional volume coming from the source (Table S1 in the supporting information). The proportionality coefficient C defines the initial order of magnitude of the plume volume and thus can be considered as a proxy of the initial volume discharged during the ejection phase. It is interesting to notice that this coefficient displays a link with the average ash eruption rate (Figure S3 in the supporting information). It appears that the AER increases with the coefficient C, following a power law trend. This observation suggests proportionality between the explosion magnitude (erupted mass) and intensity, at least for the ash fraction.

Sakurajima plume volumes range from 10^6 to 10^8 m^3 within the first 40 s of explosions, in-line with estimations for other Vulcanian plumes such as those of Santiaguito volcano (Guatemala), attaining volumes of 7×10^7 and 2.2×10^5 m^3 after 24 and 15 s, respectively (De Angelis et al., 2016; Yamamoto et al., 2008). Results for Stromboli, 10^2–10^5 m^3 in 1 to 40 s, are also comparable with the 10^2–10^4 m^3 in 10 to 12 s of Delle Donne and Ripepe (2012).

5.2.2. Ash Eruption Rate

In literature, mass eruption rate (MER) can be inferred from observed volcanic plume height (e.g., Mastin, 2007; Sparks et al., 1997) and theoretical/computational inversions (e.g., Costa et al., 2016). Most applications of these methods assume steady state plumes (Morton et al., 1956) and concern Vulcanian to Plinian eruptions (Mastin, 2007). MER can also be derived from tephra deposits and estimated eruption duration (e.g., Andronico et al., 2013; Pioli et al., 2014), but these methods neglect the erupted mass of gas and of tephra that are not mapped (e.g., large clasts that fall back into the vent) or not accounted by deposit extrapolation methods. In addition, most of the current MER estimates provide time-averaged values.

In this study, we use transient volcanic plumes to provide a first estimate of the eruption rate of ash from Strombolian and Vulcanian explosions, time resolved at a subsecond scale. These two eruption styles typically generate different gas-ash-bombs proportions. Consequently, by focusing only on the ash mass of the plume, we underestimate the total erupted mass by different amounts in the different explosions. However, as mentioned in section 2, all the transient plumes analyzed in this study were specifically chosen to be notably ash rich.

The methodology used in this study is, in principle, suitable to provide time-resolved AER from both steady and unsteady plumes without any a priori assumptions on vent diameter and particle density. Our AER method requires detailed observation on the rise velocity of the plume, an estimate/assumption of plume temperature, and an estimation of gas species proportions inside the plume and is largely dependent on the exit velocity estimation at the vent. We also assume a homogeneous concentration of ash throughout the plume, which may not be the case (Yamamoto et al., 2008).

Time-resolved data (Figure 7) reveal that AER may fluctuate as much as 1 order of magnitude in a matter of seconds. Instantaneous values for Sakurajima (Sa_8) even exceed literature reference for Plinian eruptions but only in the first second of the explosions. The error range we calculated reaches up to more than 150%. This relatively large error, however, must be viewed in the context of the order-of-magnitude variations that AER displays. Comparing our AER results with previous MER estimates of the same volcanoes, and keeping in mind the above assumptions and limitations, it appears that Sakurajima's explosions range in between Vulcanian and Plinian MER references, while Fuego and Stromboli show variations in between Strombolian and violent Strombolian references, with higher values for Stromboli (Cioni et al., 2015; Clarke et al., 2015; Mastin et al., 2009; Pioli et al., 2008; Taddeucci et al., 2015).

In Iguchi (2016), a detailed overview of the mass of ash erupted by explosion at Sakurajima volcano between 2008 and 2013 is provided. From this study, we use the mass of ash from individual eruptions from December 2010 and the monthly mass of erupted ash from July 2013 (corresponding to our recording period). The minimum and maximum mass of ash from individual explosions from December 2010 is 0.5×10^6 kg and 2.7×10^7 kg, respectively. Dividing these values by the minimum and maximum ejection duration estimated from our videos (9.5 and 49.6 s), we obtain an approximation of the range of time-averaged ash eruption rate of 1.0×10^4 to 2.8×10^6 kg/s. For July 2013, the monthly ash mass (1.07×10^9 kg) has been divided by the monthly number of explosions (80), obtaining an average mass of ash per explosion over this period. Then, we again estimated the range of time-averaged ash eruption rate using our minimum and maximum ejection durations and we obtained 2.7×10^5 and 1.4×10^6 kg/s. The time-averaged AER for Sakurajima volcano that we obtained integrating our time-resolved AER values ranges between 1.85×10^5 and 2.87×10^6 kg/s (Table 2), in good agreement with the December 2010 and July 2013 values obtained from Iguchi (2016). Our AER values are also in good agreement with MER estimates obtained via infrasound data at Sakurajima volcano during the same period (Kim et al., 2015). Using their volumetric flux and average plume density (Ripepe et al., 2013), their estimated MER peaks at 6.1×10^6 kg/s. This results is logically higher than our estimation since it accounts for the total erupted mass.

Pioli et al. (2014) reported fallout masses of major events at Stromboli volcano ranging between 10^4 and 10^6 kg. These events, even though classified as "major explosions," displayed plumes rising only up to

200 m (Pioli et al., 2014), which corresponds to the plume height range observed in our records for Stromboli and Fuego volcanoes (Figure 6a). Our ash mass estimations per event range between 10^3 and 10^5 kg, which appears to be in good agreement with Pioli et al. (2014). The authors of this study also provided estimations of mass discharge rates based on tephra mass load and neglecting the mass of gas and of unmapped bombs. Their results cluster around 10^4 kg/s, while our values range between 10^2 and 10^4 kg/s. Other studies, such as Rosi et al. (2013), showed that normal activity at Stromboli corresponds to fallout mass discharge rates of 10^2–10^3 kg/s. Our AER estimations for Stromboli and Fuego volcanoes seem to be in good agreement with previous studies on Strombolian activity. It is important to keep in mind that explosions from Stromboli volcano studied here correspond to ash-rich Type 2 explosions. It is thus logical to obtain AER ranging in the uppermost MER values of normal Strombolian events, since a significant part of the total erupted mass is composed of ash.

Once again, average values obtained at Sakurjima, Stromboli, and Fuego are comparable with Clarke et al. (2015) and Taddeucci et al. (2015) for Vulcanian and Strombolian eruptions. When compared with other eruption rate estimations at Sakurajima and Stromboli volcanoes (e.g., Iguchi, 2016; Pioli et al., 2014; Rosi et al., 2013), our AER values appear to be in good agreement with them, with the advantage of being time resolved.

Considering the final height reached by the respective plumes, some of the values of AER we show are relatively high, exceeding, over few tenth of seconds, values for Subplinian and Plinian explosions (Mastin et al., 2009). This observation highlights the role of both ejection duration and MER fluctuations on the rise of transient volcanic plumes. For example, our Sakurajima values (duration about 30 s, AER up to 10^6 kg/s with peaks up to 10^7 kg/s, and final plume height up to 4,000 m), which agree with those of Iguchi (2016), contrast with those from the June 1992 eruption of Mont Spurr, where a similar MER of 2×10^6 kg/s, but sustained over a much longer duration of more than 4 h, resulted in an ash plume with a final height of 11.3 km (Mastin et al., 2009).

It is also interesting to note that our AER estimations combined with MER values from literature can provide information about the respective ash to gas/bombs proportions during Strombolian and Vulcanian explosions. These kind of comparisons would provide useful information that could allow new understanding of transient plume dynamics and will be the object of future work.

6. Conclusion

By the use of high-speed, thermal, and high-resolution videos we parameterized the initial evolution of Strombolian- to Vulcanian-style eruptive plumes for their morphology, rise velocity, velocity field, volume, and apparent surface temperature.

It appears that the initial evolution of such plumes is fundamentally controlled by the time-space features of individual ejection pulses at the eruptive vent (i.e., their number, duration, frequency, intensity, angle, and source vent). The connection between ejection pulses and plume features seems to hold true for all our study cases, which encompass a variety of eruption styles and plume heights and morphologies. It remains open to question how much these observations can be extended to sustained eruptions, for which the occurrence of pulses is less documented, and how much our observations on the initial development of plumes may be expanded to later stages. However, these results stress the need for new experimental and numerical studies applying different and complex discharge histories in order to (i) predict the time evolution of transient plumes and associated hazards and (ii) retrieve eruptive parameters at the vent from plume measurements.

Future perspectives opened by this study also include (1) quantification of other controlling factors on plume evolution (including the presence of bomb "swarms"), (2) time-resolved ash eruption rate measurements, (3) applicability of optical flow for plume parameterization, and (4) refined measurements of air entrainment.

Acknowledgments
Data supporting this work are available in the supporting information (ms01–ms11) and at INGV Roma—Department of Seismology and Tectonophysics, HP-HT lab. This work is supported by the VERTIGO Marie Curie ITN, funded through the European Seventh Framework Programme (FP7 2007–2013) under grant agreement 607905. The authors would like to thank everybody who participated to the field campaigns.

References

Abdel-Rahman, A. A., Chakroun, W., & Al-Fahed, S. F. (1997). LDA measurements in the turbulent round jet. *Mechanics Research Communications*, *24*(3), 277–288. https://doi.org/10.1016/S0093-6413(97)00025-6

Abramoff, M. D., Magalhães, P. J., & Ram, S. J. (2004). Image processing with ImageJ. *Biophotonics International*, *11*, 36–42. Retrieved from http://dspace.library.uu.nl/handle/1874/204900, Accessed 26 September 2016.

Aiuppa, A., Bertagnini, A., Métrich, N., Moretti, R., Di Muro, A., Liuzzo, M., & Tamburello, G. (2010). A model of degassing for Stromboli volcano. *Earth and Planetary Science Letters*, *295*, 195–204. https://doi.org/10.1016/j.epsl.2010.03.040

Andronico, D., Taddeucci, J., Cristaldi, A., Miraglia, L., Scarlato, P., & Gaeta, M. (2013). The 15 March 2007 paroxysm of Stromboli: Video-image analysis, and textural and compositional features of the erupted deposit. *Bulletin of Volcanology*, *75*(7), 733. https://doi.org/10.1007/s00445-013-0733-2

Baker, S., Scharstein, D., Lewis, J. P., Roth, S., Black, M. J., & Szeliski, R. (2011). A database and evaluation methodology for optical flow. *International Journal of Computer Vision*, *92*, 1–31. https://doi.org/10.1007/s11263-010-0390-2

Barnie, T., Bombrun, M., Burton, M. R., Harris, A., & Sawyer, G. (2015). Quantification of gas and solid emissions during Strombolian explosions using simultaneous sulphur dioxide and infrared camera observations. *Journal of Volcanology and Geothermal Research*, *300*, 167–174. https://doi.org/10.1016/j.jvolgeores.2014.10.003

Blackburn, E. A., Wilson, L., & Sparks, R. S. J. (1976). Mechanisms and dynamics of Strombolian activity. *Journal of the Geological Society*, *132*(4), 429–440. https://doi.org/10.1144/gsjgs.132.4.0429

Bogusławski, L., & Popiel, C. O. (1979). Flow structure of the free round turbulent jet in the initial region. *Journal of Fluid Mechanics*, *90*(03), 531–539. https://doi.org/10.1017/S0022112079002378

Bonadonna, C., Pistolesi, M., Cioni, R., Degruyter, W., Elissondo, M., & Baumann, V. (2015). Dynamics of wind-affected volcanic plumes: The example of the 2011 Cordón Caulle eruption, Chile. *Journal of Geophysical Research: Solid Earth*, *120*, 2242–2261. https://doi.org/10.1002/2014JB011478

Burton, M., Allard, P., Muré, F., & Spina, A. L. (2007). Magmatic gas composition reveals the source depth of slug-driven Strombolian explosive activity. *Science*, *317*, 227–230. https://doi.org/10.1126/science.1141900

Capponi, A., Taddeucci, J., Scarlato, P., & Palladino, D. M. (2016). Recycled ejecta modulating Strombolian explosions. *Bulletin of Volcanology*, *78*(2), 13. https://doi.org/10.1007/s00445-016-1001-z

Chojnicki, K. N., Clarke, A. B., Adrian, R. J., & Phillips, J. C. (2014). The flow structure of jets from transient sources and implications for modeling short-duration explosive volcanic eruptions. *Geochemistry, Geophysics, Geosystems*, *15*(12), 4831–4845. https://doi.org/10.1002/2014gc005471

Chojnicki, K. N., Clarke, A. B., Phillips, J. C., & Adrian, R. J. (2015a). Rise dynamics of unsteady laboratory jets with implications for volcanic plumes. *Earth and Planetary Science Letters*, *412*(0), 186–196. https://doi.org/10.1016/j.epsl.2014.11.046

Chojnicki, K., Clarke, A., Phillips, J., & Adrian, R. (2015b). The evolution of volcanic plume morphology in short-lived eruptions. *Geology*, *43*(8), 707–710. https://doi.org/10.1130/G36642.1

Chouet, B., Hamisevicz, N., & McGetchin, T. R. (1974). Photoballistics of volcanic jet activity at Stromboli, Italy. *Journal of Geophysical Research*, *79*(32), 4961–4976. https://doi.org/10.1029/JB079i032P04961

Cigala, V., Kueppers, U., Peña Fernández, J. J., Taddeucci, J., Sesterhenn, J., & Dingwell, D. B. (2017). The dynamics of volcanic jets: Temporal evolution of particles exit velocity from shock-tube experiments. *Journal of Geophysical Research: Solid Earth*, *122*, 6031–6045. https://doi.org/10.1002/2017JB014149

Cioni, R., Pistolesi, M., & Rosi, M. (2015). Plinian and Subplinian eruptions. In *The Encyclopedia of Volcanoes* (pp. 519–535). Amsterdam: Elsevier. https://doi.org/10.1016/B978-0-12-385938-9.00029-8

Clarke, A. B., Voight, B., Neri, A., & Macedonio, G. (2002). Transient dynamics of Vulcanian explosions and column collapse. *Nature*, *415*(6874), 897–901. https://doi.org/10.1038/415897a

Clarke, A. B., Ongaro, T. E., & Belousov, A. (2015). Vulcanian eruptions. In *The Encyclopedia of Volcanoes* (pp. 505–518). Amsterdam: Elsevier. https://doi.org/10.1016/B978-0-12-385938-9.00028-6

Costa, A., Suzuki, Y. J., Cerminara, M., Devenish, B. J., Ongaro, T. E., Herzog, M., … Bonadonna, C. (2016). Results of the eruptive column model inter-comparison study. *Journal of Volcanology and Geothermal Research*, *326*, 2–25. https://doi.org/10.1016/j.jvolgeores.2016.01.017

De Angelis, S. D., Lamb, O. D., Lamur, A., Hornby, A. J., von Aulock, F. W., Chigna, G., … Rietbrock, A. (2016). Characterization of moderate ash-and-gas explosions at Santiaguito volcano, Guatemala, from infrasound waveform inversion and thermal infrared measurements. *Geophysical Research Letters*, *43*(12), 6220–6227. https://doi.org/10.1002/2016GL069098

Del Bello, E., Llewellin, E. W., Taddeucci, J., Scarlato, P., & Lane, S. J. (2012). An analytical model for gas overpressure in slug-driven explosions: Insights into Strombolian volcanic eruptions. *Journal of Geophysical Research*, *117*, B02206. https://doi.org/10.1029/2011JB008747

Delle Donne, D., & Ripepe, M. (2012). High-frame rate thermal imagery of Strombolian explosions: Implications for explosive and infrasonic source dynamics. *Journal of Geophysical Research*, *117*, B09206. https://doi.org/10.1029/2011JB008987

Dürig, T., Gudmundsson, M. T., & Dellino, P. (2015). Reconstruction of the geometry of volcanic vents by trajectory tracking of fast ejecta—The case of the Eyjafjallajökull 2010 eruption (Iceland). *Earth, Planets and Space*, *67*(1), 64. https://doi.org/10.1186/s40623-015-0243-x

Francalanci, L., Manetti, P., & Peccerillo, A. (1989). Volcanological and magmatological evolution of Stromboli volcano (Aeolian Islands): The roles of fractional crystallization, magma mixing, crustal contamination and source heterogeneity. *Bulletin of Volcanology*, *51*(5), 355–378. https://doi.org/10.1007/BF01056897

Freund, J. B., Lele, S. K., & Moin, P. (2000). Numerical simulation of a Mach 1.92 turbulent jet and its sound field. *AIAA Journal*, *38*(11), 2023–2031. https://doi.org/10.2514/2.889

Gaudin, D., Taddeucci, J., Scarlato, P., Moroni, M., Freda, C., Gaeta, M., & Palladino, D. M. (2014). Pyroclast tracking velocimetry illuminates bomb ejection and explosion dynamics at Stromboli (Italy) and Yasur (Vanuatu) volcanoes. *Journal of Geophysical Research: Solid Earth*, *119*, 5384–5397. https://doi.org/10.1002/2014JB011096

Gaudin, D., Taddeucci, J., Scarlato, P., Bello, E., Ricci, T., Orr, T., … Bucci, A. (2017). Integrating puffing and explosions in a general scheme for Strombolian-style activity. *Journal of Geophysical Research: Solid Earth*, *122*, 1860–1875. https://doi.org/10.1002/2016JB013707

Global Volcanism Program (2012). Report on Fuego (Guatemala). In S. K. Sennert (Ed.), *Weekly volcanic activity report, 11 January-17 January 2012*. Smithsonian Institution and US Geological Survey.

Harris, A. (2013). *Thermal remote sensing of active volcanoes: A user's manual*. New York: Cambridge University Press. https://doi.org/10.1017/CBO9781139029346

Harris, A., & Ripepe, M. (2007). Synergy of multiple geophysical approaches to unravel explosive eruption conduit and source dynamics—A case study from Stromboli. *Chemie der Erde-Geochemistry*, *67*, 1–35. https://doi.org/10.1016/j.chemer.2007.01.003

Harris, A. J. L., Ripepe, M., & Hughes, E. A. (2012). Detailed analysis of particle launch velocities, size distributions and gas densities during normal explosions at Stromboli. *Journal of Volcanology and Geothermal Research*, *231-232*, 109–131. https://doi.org/10.1016/j.jvolgeores.2012.02.012

Harris, A. J. L., Delle Donne, D., Dehn, J., Ripepe, M., & Worden, A. K. (2013). Volcanic plume and bomb field masses from thermal infrared camera imagery. *Earth and Planetary Science Letters*, *365*, 77–85. https://doi.org/10.1016/j.epsl.2013.01.004

Hussein, H. J., Capp, S. P., & George, W. K. (1994). Velocity measurements in a high-Reynolds-number, momentum-conserving, axisymmetric, turbulent jet. *Journal of Fluid Mechanics*, *258*(1), 31–75. https://doi.org/10.1017/S002211209400323X

Iguchi, M. (2016). Method for real-time evaluation of discharge rate of volcanic ash: Case study on intermittent eruptions at the Sakurajima volcano, Japan (special issue on integrated study on mitigation of multimodal disasters caused by ejection of volcanic products). *Journal of Disaster Research*, *11*(1), 4–14. https://doi.org/10.20965/jdr.2016.p0004

Iguchi, M., Yakiwara, H., Tameguri, T., Hendrasto, M., & Hirabayashi, J. (2008). Mechanism of explosive eruption revealed by geophysical observations at the Sakurajima, Suwanosejima and Semeru volcanoes. *Journal of Volcanology and Geothermal Research*, *178*, 1–9. https://doi.org/10.1016/j.jvolgeores.2007.10.010

Iguchi, M., Tameguri, T., Ohta, Y., Ueki, S., & Nakao, S. (2013). Characteristics of volcanic activity at Sakurajima volcano's Showa crater during the period 2006 to 2011. *Bulletin of the Volcanological Society of Japan*, *58*(1), 115–135.

Iqbal, M. O., & Thomas, F. O. (2007). Coherent structure in a turbulent jet via a vector implementation of the proper orthogonal decomposition. *Journal of Fluid Mechanics*, *571*, 281–326. https://doi.org/10.1017/S0022112006003351

Ishihara, K. (1985). Dynamical analysis of volcanic explosion. *Journal of Geodynamics*, *3*(3–4), 327–349. https://doi.org/10.1016/0264-3707(85)90041-9

Japan Meteorological Agency (2016). 平成 28 年(2016 年)の桜島の火山活動 volcanic activity of Sakurajima in Heisei 28 (2016). Retrieved from http://www.data.jma.go.jp/svd/vois/data/tokyo/STOCK/monthly_v-act_doc/fukuoka/2016y/506_16y.pdf

Johnson, J. B., Aster, R. C., & Kyle, P. R. (2004). Volcanic eruptions observed with infrasound. *Geophysical Research Letters*, *31*, L14604. https://doi.org/10.1029/2004GL020020

Johnson, J. B., Harris, A. J. L., Sahetapy-Engel, S. T. M., Wolf, R., & Rose, W. I. (2004). Explosion dynamics of pyroclastic eruptions at Santiaguito volcano. *Geophysical Research Letters*, *31*, L06610. https://doi.org/10.1029/2003GL019079

Kim, K., Fee, D., Yokoo, A., & Lees, J. M. (2015). Acoustic source inversion to estimate volume flux from volcanic explosions. *Geophysical Research Letters*, *42*(13), 5243–5249. https://doi.org/10.1002/2015GL064466

Kitamura, S., & Sumita, I. (2011). Experiments on a turbulent plume: Shape analyses. *Journal of Geophysical Research*, *116*, B03208. https://doi.org/10.1029/2010JB007633

Leduc, L., Gurioli, L., Harris, A., Colò, L., & Rose-Koga, E. F. (2015). Types and mechanisms of Strombolian explosions: Characterization of a gas-dominated explosion at Stromboli. *Bulletin of Volcanology*, *77*(1), 1–15. https://doi.org/10.1007/s00445-014-0888-5

Lyons, J. J., & Waite, G. P. (2011). Dynamics of explosive volcanism at Fuego volcano imaged with very long period seismicity. *Journal of Geophysical Research*, *116*, B09303. https://doi.org/10.1029/2011JB008521

Lyons, J. J., Waite, G. P., Rose, W. I., & Chigna, G. (2010). Patterns in open vent, Strombolian behavior at Fuego volcano, Guatemala, 2005–2007. *Bulletin of Volcanology*, *72*, 1–15. https://doi.org/10.1007/s00445-009-0305-7

Marchetti, E., Ripepe, M., Harris, A. J. L., & Delle Donne, D. (2009). Tracing the differences between Vulcanian and Strombolian explosions using infrasonic and thermal radiation energy. *Earth and Planetary Science Letters*, *279*, 273–281. https://doi.org/10.1016/j.epsl.2009.01.004

Mastin, L. G. (2007). A user-friendly one-dimensional model for wet volcanic plumes. *Geochemistry, Geophysics, Geosystems*, *8*, Q03014. https://doi.org/10.1029/2006GC001455

Mastin, L. G., Guffanti, M., Servranckx, R., Webley, P., Barsotti, S., Dean, K., … Waythomas, C. F. (2009). A multidisciplinary effort to assign realistic source parameters to models of volcanic ash-cloud transport and dispersion during eruptions. *Journal of Volcanology and Geothermal Research*, *186*, 10–21. https://doi.org/10.1016/j.jvolgeores.2009.01.008

Morton, B., Taylor, G., & Turner, J. (1956). *Turbulent gravitational convection from maintained and instantaneous sources* (Vol. 234, pp. 1–23). London: The Royal Society.

Neri, A., Esposti Ongaro, T., Macedonio, G., & Gidaspow, D. (2003). Multiparticle simulation of collapsing volcanic columns and pyroclastic flow. *Journal of Geophysical Research*, *108*(B4), 2202. https://doi.org/10.1029/2001JB000508

Panchapakesan, N. R., & Lumley, J. L. (1993). Turbulence measurements in axisymmetric jets of air and helium. Part 1. Air jet. *Journal of Fluid Mechanics*, *246*(1), 197–223. https://doi.org/10.1017/S0022112093000096

Patrick, M. R. (2007). Dynamics of Strombolian ash plumes from thermal video: Motion, morphology, and air entrainment. *Journal of Geophysical Research*, *112*, B06202. https://doi.org/10.1029/2006JB004387

Patrick, M., Harris, A. L., Ripepe, M., Dehn, J., Rothery, D., & Calvari, S. (2007). Strombolian explosive styles and source conditions: Insights from thermal (FLIR) video. *Bulletin of Volcanology*, *69*, 769–784. https://doi.org/10.1007/s00445-006-0107-0

Peña Fernández, J. J., & Sesterhenn, J. (2017). Compressible starting jet: Pinch-off and vortex ring–trailing jet interaction. *Journal of Fluid Mechanics*, *817*, 560–589. https://doi.org/10.1017/jfm.2017.128

Pioli, L., Erlund, E., Johnson, E., Cashman, K., Wallace, P., Rosi, M., & Delgado Granados, H. (2008). Explosive dynamics of violent Strombolian eruptions: The eruption of Parícutin volcano 1943–1952 (Mexico). *Earth and Planetary Science Letters*, *271*, 359–368. https://doi.org/10.1016/j.epsl.2008.04.026

Pioli, L., Pistolesi, M., & Rosi, M. (2014). Transient explosions at open-vent volcanoes: The case of Stromboli (Italy). *Geology*, *42*(10), 863–866. https://doi.org/10.1130/G35844.1

Quinn, W. R. (2006). Upstream nozzle shaping effects on near field flow in round turbulent free jets. *European Journal of Mechanics - B/Fluids*, *25*, 279–301. https://doi.org/10.1016/j.euromechflu.2005.10.002

Ripepe, M., Rossi, M., & Saccorotti, G. (1993). Image processing of explosive activity at Stromboli. *Journal of Volcanology and Geothermal Research*, *54*(3-4), 335–351. https://doi.org/10.1016/0377-0273(93)90071-X

Ripepe, M., Bonadonna, C., Folch, A., Delle Donne, D., Lacanna, G., Marchetti, E., & Höskuldsson, A. (2013). Ash-plume dynamics and eruption source parameters by infrasound and thermal imagery: The 2010 Eyjafjallajökull eruption. *Earth and Planetary Science Letters*, *366*, 112–121. https://doi.org/10.1016/j.epsl.2013.02.005

Rosi, M., Pistolesi, M., Bertagnini, A., Landi, P., Pompilio, M., & Roberto, A. D. (2013). Chapter 14 Stromboli volcano, Aeolian Islands (Italy): Present eruptive activity and hazards. *Geological Society of London's Memoirs*, *37*(1), 473–490. https://doi.org/10.1144/M37.14

Sahetapy-Engel, S. T., & Harris, A. J. L. (2009). Thermal-image-derived dynamics of vertical ash plumes at Santiaguito volcano, Guatemala. *Bulletin of Volcanology*, *71*, 827–830. https://doi.org/10.1007/s00445-009-0284-8

Sawyer, G. M., & Burton, M. R. (2006). Effects of a volcanic plume on thermal imaging data. *Geophysical Research Letters*, *33*, L14311. https://doi.org/10.1029/2005GL025320

Scharff, L., Hort, M., & Varley, N. R. (2015). Pulsed Vulcanian explosions: A characterization of eruption dynamics using Doppler radar. *Geology*, *43*(11), 995–998. https://doi.org/10.1130/G36705.1

Spampinato, L., Calvari, S., Oppenheimer, C., & Boschi, E. (2011). Volcano surveillance using infrared cameras. *Earth-Science Reviews*, *106*, 63–91. https://doi.org/10.1016/j.earscirev.2011.01.003

Sparks, R. S. J., Bursik, M., Carey, S. N., Gilbert, J. S., Glaze, L. S., Sigurdsson, H., & Woods, A. W. (1997). *Volcanic Plumes*. Chichester, UK: John Wiley.

Sun, D., Roth, S., & Black, M. J. (2010). Secrets of optical flow estimation and their principles. In *2010 IEEE computer society conference on computer vision and pattern recognition* (pp. 2432–2439).

Sun, D., Roth, S., & Black, M. J. (2014). A quantitative analysis of current practices in optical flow estimation and the principles behind them. *International Journal of Computer Vision*, *106*(2), 115–137. https://doi.org/10.1007/s11263-013-0644-x

Suwa, H., Suzuki, Y. J., & Yokoo, A. (2014). Estimation of exit velocity of volcanic plume from analysis of vortex structures. *Earth and Planetary Science Letters*, *385*, 154–161. https://doi.org/10.1016/j.epsl.2013.10.032

Taddeucci, J., Scarlato, P., Capponi, A., Del Bello, E., Cimarelli, C., Palladino, D. M., & Kueppers, U. (2012). High-speed imaging of Strombolian explosions: The ejection velocity of pyroclasts. *Geophysical Research Letters*, *39*, L02301. https://doi.org/10.1029/2011GL050404

Taddeucci, J., Edmonds, M., Houghton, B., James, M. R., & Vergniolle, S. (2015). Hawaiian and Strombolian eruptions. In *The Encyclopedia of Volcanoes* (pp. 485–503). Amsterdam: Elsevier. https://doi.org/10.1016/B978-0-12-385938-9.00027-4

Turner, J. S. (1962). The "starting plume" in neutral surroundings. *Journal of Fluid Mechanics*, *13*(03), 356–368. https://doi.org/10.1017/S0022112062000762

Turner, J. S. (1969). Buoyant plumes and thermals. *Annual Review of Fluid Mechanics*, *1*(1), 29–44. https://doi.org/10.1146/annurev.fl.01.010169.000333

Turner, J. S. (1979). *Buoyancy effects in fluids*. New York: Cambridge University Press.

Valade, S., Harris, A., & Cerminara, M. (2014). Plume ascent tracker: Interactive MATLAB software for analysis of ascending plumes in image data. *Computational Geosciences*, *66*, 132–144. https://doi.org/10.1016/j.cageo.2013.12.015

Webb, E. B., Varley, N. R., Pyle, D. M., & Mather, T. A. (2014). Thermal imaging and analysis of short-lived Vulcanian explosions at Volcán de Colima, Mexico. *Journal of Volcanology and Geothermal Research*, *278-279*, 132–145. https://doi.org/10.1016/j.jvolgeores.2014.03.013

Wilson, L., Sparks, R. S. J., Huang, T. C., & Watkins, N. D. (1978). The control of volcanic column heights by eruption energetics and dynamics. *Journal of Geophysical Research*, *83*(B4), 1829–1836. https://doi.org/10.1029/JB083iB04p01829

Woods, A. W. (1988). The fluid dynamics and thermodynamics of eruption columns. *Bulletin of Volcanology*, *50*(3), 169–193. https://doi.org/10.1007/BF01079681

Xu, G., & Antonia, R. (2002). Effect of different initial conditions on a turbulent round free jet. *Experiments in Fluids*, *33*, 677–683. https://doi.org/10.1007/s00348-002-0523-7

Yamamoto, H., Watson, I. M., Phillips, J. C., & Bluth, G. J. (2008). Rise dynamics and relative ash distribution in Vulcanian eruption plumes at Santiaguito volcano, Guatemala, revealed using an ultraviolet imaging camera. *Geophysical Research Letters*, *35*, L08314. https://doi.org/10.1029/2007GL032008

Yuan, A. T. E., McNutt, S. R., & Harlow, D. H. (1984). Seismicity and eruptive activity at Fuego volcano, Guatemala: February 1975–January 1977. *Journal of Volcanology and Geothermal Research*, *21*(3-4), 277–296. https://doi.org/10.1016/0377-0273(84)90026-X

Zanon, V., Neri, M., & Pecora, E. (2009). Interpretation of data from the monitoring thermal camera of Stromboli volcano (Aeolian Islands, Italy). *Geological Magazine*, *146*, 591–601. https://doi.org/10.1017/S0016756809005937